Local Up-Sampling and Morphological Analysis of Low-Resolution Magnetic Resonance Images

Mattia Natali[a], Giulio Tagliafico[a], Giuseppe Patanè[a]

[a]*CNR-IMATI, Genova - Italy*
`{natali,tagliafico,patane}@ge.imati.cnr.it`

Abstract

Limitations in the resolution of acquired images, which are due to sensor manufacturing and acquisition conditions, are reduced with the help of algorithms that enhance the spatial resolution by assigning pixel values that are interpolated or approximated from known pixels. We propose a variant of the moving least-squares approximation for image up-sampling, with a specific focus on biomedical MR images. For each evaluation point, we locally compute the best approximation by minimizing a weighted least-squares error between the input data and their approximation with an implicit function. The proposed approach provides a continuous approximation, an accuracy and extrapolation capabilities higher than previous work, and a lower computational cost. As main application, we consider the up-sampling of low field MR images, where the volumetric and meshless properties of the approximation allow us to easily process images with anisotropic voxel size by rescaling the image and inter-slices resolution. Finally, we include the resolution rescaling into a pipeline that performs a morphological characterization of 3D anatomical districts, which has been developed with a focus on rheumatoid arthritis evolution and provides a more accurate segmentation as an input to quantitative analysis.

Keywords: Biomedical informatics and mathematics, computer-aided diagnosis, image segmentation and feature extraction, image up-sampling and enhancement, quantitative analysis, moving least-squares approximation.

---

1. Introduction

Imaging hardware, acquisition methodologies and time, overlap of different tissues, physiological and pathological phenomena generally limit the image resolution. To partially overcome these drawbacks, a relatively small number of 2D slices is acquired at the cost of a larger slice thickness and space between slices; as a result, the resolution in the slice direction is lower than the resolution in the acquisition plane. Furthermore, noise, non-uniform intensity, and partial volume averaging generally affect anisotropic MR images, make their analysis error-prone, and generate blurring effects or "distorted" reconstructions of the underlying geometries. For instance, a single tissue might have a non-uniform intensity over the acquired images, due to a different homogeneity of the tissue itself, or some pixels might show an average intensity in those regions where different tissues overlap. All these elements are further complicated by the tissue variability among individuals and their morphological complexity. In this context, *image up-sampling* tackles the problem of increasing the resolution of an image, or more generally a set of images composing a volumetric data set, by preserving its main features (e.g., sharp edges, textures) and removing artifacts (e.g., blurring, pixel blocking). In medical applications, image up-sampling is crucial for segmentation and analysis, where algorithms are typically limited by the data resolution, anisotropy, and blurring. In all these cases, the higher the image resolution is, the more accurate the analysis is (e.g., segmentation, quantitative and morphological analysis). Main features of image up-sampling are processing speed for prompt user interaction, sharpness on the whole image, preservation of image textures, low influence of parameters in the results, and low memory consumption. Visual properties to be preserved are the image contrast, the absence of blocky regions, and the contour sharpness.

The *quantitative analysis* of low resolution images is generally affected by their transformation to a different space or representation (e.g., through image registration, interpolation, segmentation, iso-surface extraction) and heavily depends on the voxel size. This situation typically happens for the segmentation of small bones and tissues in musculo-skeletal districts. To overcome these limitations, the up-sampling of low-resolution MR images guarantees a more accurate segmentation and quantitative analysis of morphological parameters [32], reduce the effect of volume variability, and improve the consistency of the results for follow-up data, thanks to a precise identification of region boundaries. These aspects are particularly relevant for the wrist sector, given the small dimension of the segmented components in comparison to the pixel dimension. Furthermore, for muscle-skeletal pathologies of joints a more accurate detection and quantification of local erosions provide a better analysis than the global volume obtained by the original images [51], which could mask the effect of a mild erosion in the early stages of the disease.

Overview and contribution. Previous work (Sect. 2) on image up-sampling satisfies only a few of the aforementioned properties, thus introducing artifacts in the up-sampled image. In this context, we propose a local variant of the moving least-squares (MLS) approximation (Sect. 3). Given a function $f:\mathcal{P}\rightarrow\mathbb{R}$, on a set $\mathcal{P}:=\{\mathbf{x}_i\}_{i=1}^{n}$ of points in $\mathbb{R}^d$, we tackle the problem of computing a smooth function $F:\mathbb{R}^d\rightarrow\mathbb{R}$, which is a linear combination of radial basis functions (RBFs), *locally* approximates the f-values, and minimizes a weighted least-squares error. For instance, for a 3D image $\{\mathbf{x}_i\}_{i=1}^{n}$ are the coordinates of the voxels, $f(\mathbf{x}_i)$ is the corresponding pixel intensity, and n is the total number of voxels in the image space. The idea behind the evaluation of $F(\mathbf{x})$ is to compute the function $F(\cdot)$ in a neighbor $\mathcal{N}_{\mathbf{x}}$ of $\mathbf{x}$ by imposing the f-values at $\mathcal{N}_{\mathbf{x}}$, instead of $\mathcal{P}$, as approximation constraints. In fact, the behavior of any continuous approximation of f at $\mathbf{x}$ is controlled by the f-values in $\mathcal{N}_{\mathbf{x}}$.

While previous work [31, 52] considers a polynomial approximation, in our approach $F(\cdot)$ is a linear combination of RBFs centered at the points of $\mathcal{P}$, whose coefficients solve a small and well-conditioned linear system. Replacing the polynomial with a radial basis provides an accuracy and extrapolation capabilities higher than previous work and allows us to apply interpolating constraints for feature preservation or least-squares conditions for noise removal. In fact, the number of local interpolating constraints is equal to the number of RBFs and no more related to a given degree of the approximating polynomial. In contrast, imposing interpolating constraints in the MLS approximation with a polynomial basis is rather difficult, as the degree of the fitting polynomial determines the number of interpolating conditions and not *viceversa*. For instance, the interpolation with a polynomial in x, y, and z of degree two or three requires ten or nineteen interpolating constraints, respectively. However, we might choose a different number of points in different neighbors, according to the variation of the f-values (e.g., pixel intensities).

Instead of applying a MLS approximation to single images, or a shape-based interpolation [40], or computing different slice orientations [82, 39, 66], the proposed approach works both in the image plane and inter slices, by taking advantage of the volumetric and meshless properties of the RBFs. In this way, we define a fully volumetric approximation of anisotropic data, enforce the consistency of the approximation through a larger number of interpolating or least-squares constraints across consecutive slices, and accurately preserve feature lines, as a matter of the interpolation constraints.

Global approximation methods [26, 61, 83, 78] solve one large linear system for the whole data and a low amount of calculation is needed to evaluate the approximating function at any spatial location. The allocation of the coefficient matrix and the numerical solver of the linear system (e.g., $O(n^3)$ or $O(n\log n)$ time for globally- or locally-supported RBFs) are the main computational bottlenecks. Our approximation solves a $k\times k$ (e.g., $20\leq k\leq 30$) linear system for each sample point in $O(k^3)$ time. Indeed, the computational cost of the MLS scheme with RBFs is generally lower than the global approximation with RBFs, reduces the memory storage, and has the same order of complexity of the polynomial MLS scheme.

Our experiments show a good performance of the local approximation induced by the Hardy's and Gaussian kernels. Thin-plate kernel approximation provides a lower approximation accuracy and feature preservation with respect to the Hardy's and Gaussian kernels, due to the ill-conditioning of the coefficient matrix in case of large up-sampling factors and higher smoothing effects. We also compare our approximation scheme with linear [80], spline [72, 79], local interpolation [59], feature-based [44], sparse [56], and total variation [74] methods. Statistics confirm that the meshless approximation outperforms the linear and polynomial methods, which can generate undesired effects, such as aliasing. The non-local up-sampling [59] exhibits a slightly better accuracy than the meshless approximation with

RBFs; however, it requires a de-noising step, several iterations to optimize the image quality, and a higher computational cost. Finally, the proposed approach provides results comparable with the feature-based, sparse, total variation methods and supports the rescaling of the resolution of anisotropic images both on the image plane and inter-slices.

The meshless up-sampling of low-resolution MR images guarantees a more accurate segmentation and quantitative analysis of morphological parameters for the hand-wrist anatomical district and a proper segmentation of the cartilage, which is not easy to achieve with low-field images [32]. To discuss these properties, we present a pipeline for the local characterization of the morphology of the bones of the wrist joint from single and follow-up images (Sect. 4). Local shape variations and distances among adjacent bones (i.e., intra-bones' space) are extracted from up-sampled MR images to detect cartilage destruction or joint space narrowing, which occur at an early stage of erosion and are followed by a substantial and massive erosion. The input to our process is a set of low-resolution images of complete joints, which are (eventually) up-sampled with the proposed approach, segmented with a geodesic active contour method [15], and associated with a semantic label.

For the analysis of a single exam (e.g., bone or complete joint), intra-bones' distances are computed as their Hausdorff distance [20] on the basis of anatomical atlases. For the analysis of series of exams, we perform a shape registration of segmented follow-up data and a local distance evaluation to identify shape changes and eroded regions. For the detection and quantification of local morphological variations (e.g., erosion) of bones with respect to its baseline, we evaluate the Hausdorff distance between the co-registered shapes. The distances between adjacent structures are mapped on the bones and their temporal variation is useful to characterize different diseases, such as cartilage destruction or other pathologies involving a geometrical modification of the joint structures. Then, the volume of each eroded part is computed and the resulting quantitative information is annotated in the segmentation.

The proposed local and more accurate erosion detection and quantification provide a better analysis than the global volume obtained by the original images [51], whose variability could mask the effect of a mild erosion, typical of the early stages of the disease. In fact [51], in the early stages the eroded volume can be of $10-20\%$ of the global volume; i.e., the same order of magnitude of the global volume uncertainty associated with low-resolution MR images. Furthermore, the small size and complex geometry of the carpal bones, whose segmentation heavily depends on the voxel size with respect to the image resolution, is an additional factor of uncertainty in both the segmentation and the morphological analysis.

Through image up-sampling, we reduce the volume variability and improve the consistency of the results for follow-up data. In fact, the segmentation algorithm works better on higher resolution images because it penetrates higher frequency features more easily and can reach the segmented object boundaries more closely. Main improvements after up-sampling include (i) a higher precision in the identification of the seed voxel used by the segmentation with geodesic active contours; (ii) a higher precision of the segmented contours and less smoothed bones; and (iii) a lower number of segmentation errors (e.g., spurious connected components) that are typically induced by a wrong selection of the seed pixels.

Finally (Sect. 5), we discuss the main limitation of the proposed approach and further applications of the morphological characterization of different anatomical districts for the analysis of degenerative pathologies and the localization of shape variations due to posture.

2. Related work

We briefly review previous work on image up-sampling (Sect. 2.1) and the morphological analysis of segmented 3D data (Sect. 2.2).

2.1. Image up-sampling

Nearest neighborhood methods [69] consider the nearest pixel and assign its value to the new point, preserve shapes of the original image, and can be applied to high magnification factors; however, they produce blocks of pixels easily detectable by human eyes. *Bilinear interpolation* uses a 2×2 neighborhood to compute a linear interpolation on each dimension of the image space [18], where the approximated value is a weighted average of the four pixel values around it. Bilinear image interpolation provides better results than nearest neighborhood methods, but it may generate undesired effects, such as jagged edges, ringing artifacts, or blurred images. *Bi-cubic* methods [3, 22] interpolate the input data using a 4×4 neighborhood, where closer pixels correspond to stronger weights. Sharp images can be obtained in this way and the computational complexity of bi-cubic methods is relatively low. Main drawbacks are ringing artifacts, blurred images as for bi-linear approaches, with no guarantee to always preserve edges.

Iterative non-local up-sampling [59] takes into account the self-similarity of medical images and assumes that the intensity value of a low-resolution image pixel is an average of the intensities of the corresponding high-resolution image in its proximity with an additive noise caused by the acquisition process. This technique requires a preliminary de-noising, where the filtered image is used as a reference during the iterative process and its up-sampled version is used as a solution for the first iteration. The constraints for patch-based non-local reconstruction are analogous to previous work [29, 67]. In [58], up-sampled images are generated with the help of a reference high-resolution image, which is provided by a high-resolution volume acquired with the same or another modality. This process requires the registration and de-noising of the initial low-resolution image and an iterative method that is constrained to a target image. Finally, image priors, genetic algorithms, and dictionary learning can be applied to guide the image up-sampling [71, 58, 45], segmentation [35], and retrieval [76].

Numerical approaches interpolate unknown pixel values with splines, or related techniques, and generally provide a high similarity matching with the original image and a lower number of undesired effects with respect to the techniques previously described. Wavelet-based interpolation [13, 17] works well for edges and their sharpness, but not for textures in the input image. Recent approaches for the reconstruction of super-resolution images apply signal processing techniques, such as the Fourier Transform or Bayesian estimator [43], to a sequence of low resolution images in order to obtain an improved result [63]. In [75], the total variation regularization has been applied to MR image super-resolution to integrate local and global image information. In [45], non-local means feature-based methods have been specialized to MR image up-sampling by combining structural information and image contrast with interpolation methods of low-resolution images.

Moving least-squares [31, 52] and *implicit* [10] *approximations*, with globally- [14] and locally-supported [83] radial basis functions [26, 61] convert heterogeneous discrete data into a meshless and smooth representation, for image synthesis [50] and surface reconstruction [34, 73, 78]. In [11], the moving least-squares approximation with a polynomial kernel is applied to combine low-resolution images in an up-sampled image. In [47], the selected kernel is exponential and the coefficients of the resulting approximation are signal-dependent. In order to avoid blurred images, which are typically induced by a polynomial approximation, an edge detection identifies sharp features to be preserved. For instance, the edge detection is applied locally and before the interpolation [46], or through a sub-pixel edge estimation [2], statistical approaches [54, 53], or the minimization of the approximation error [88]. In particular, the edge-directed interpolation with RBFs [54] adapts the local approximation to the edge orientation and it is computed according to a pre-defined set of stencils for faces and edge points.

Shape-based interpolation [68] with MLS approximation encodes the intrinsic manifold structure [55] through the spectral properties of the graph Laplacian and applies interpolating constraints [33, 40, 41, 42, 66], slice matching [39], feature constraints [54] and directional coherence [81, 82]. An interpolation constrained to the structural information of a high-resolution image with a different contrast [45] has been applied to brain images. In this case, laminar structures are assumed to be part of the image and are involved in the definition of a similarity measure. The main difference with respect to our approach is that a reference high-resolution image is introduced into the process to reproduce similar structures. In [71], the resolution of brain images is enhanced by extracting higher frequency details from high-resolution anatomical templates, which provide anatomical inter-modality priors. This technique does not apply interpolation constraints and requires a time-consuming registration of the input with the reference image. In [57], the adaptive method is based on a least-squares approximation and is steered by the edges; in this way, the interpolated high-resolution image is less affected by artifacts along contours and the edge information is implicitly retrieved from covariance. As main applications, we mention image registration [16] and surface reconstruction [21].

Sparse representations and manifold regularized sparse learning have been successfully applied to image super-resolution. More precisely, in [87] the super-resolution reconstruction of low resolution MR images is based on a joint sparse representation through a ℓ_1 norm minimization and suppresses blurring effects with sparse priors. Most of the interpolation methods for image super-resolution disregards that a low resolution pixel

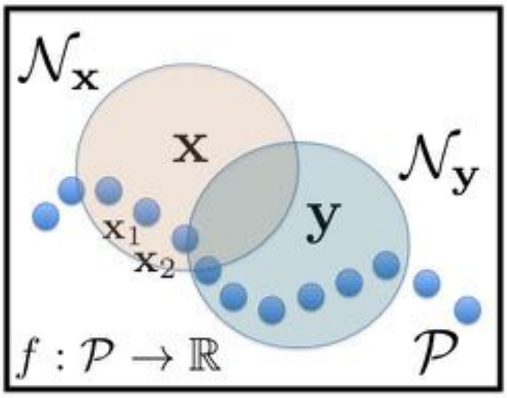

Figure 1: *Given a discrete function* $f:\mathcal{P}\rightarrow\mathbb{R}$ *on a set of points* $\mathcal{P}:=\{\mathbf{x}_i\}_{i=1}^n$ *of points of* $\mathbb{R}^d$*, we compute a smooth function* $F:\mathbb{R}^d\rightarrow\mathbb{R}$*, whose value* $F(\mathbf{x})$ *at a given sample point* $\mathbf{x}$ *is computed by locally interpolating/approximating the* f*-values at the points of* $\mathcal{P}$ *belonging to a neighbor* $\mathcal{N}_\mathbf{x}$ *of* $\mathbf{x}$*. The function* F *in* $\mathcal{N}_\mathbf{x}$ *is defined as a linear combination of RBFs centered at the points of* $\mathcal{N}_\mathbf{x}$ *and is continuous at any point* $\mathbf{x}$*; i.e.,* $\lim_{\mathbf{y}\rightarrow\mathbf{x}}F(\mathbf{y})=F(\mathbf{x})$.

can be considered as a weighted average of high resolution pixels inside it and are typically affected by blurred edges and complex textures. To avoid these artifacts, the resolution and contrast of MR images can be improved by fusing multiple 2D slices with different directions [74, 63] and feature-based approaches [44]. Over-complete dictionaries for resolution enhancement of MR images have been defined in [85, 24], and in [56] manifold regularized sparse learning has been applied to preserve the intrinsic structure between MR images and to exploit the intra-patient priors. In fact, intra-patient MR images [71, 12, 84] are typically available in follow-up monitoring of degenerate pathologies or when different acquisition parameters are chosen to acquire a series of scans.

Methods based on partial differential equations [49] are suitable for edge preservation and combine linear interpolation with fuzzy logic to overcome the main disadvantages given by simple linear image interpolation approaches. Moreover, these methods can be improved with an edge-oriented refinement to better preserve boundaries, which is usually achieved by selecting different neighbors with different shapes.

(a) Input 256 × 256

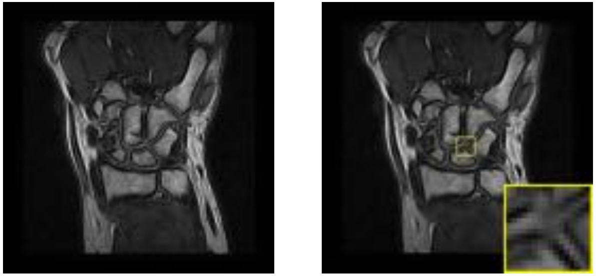

(b) Input 128×128 (c) Gauss 256×256 $MRE=97.63, PSNR=28.23$

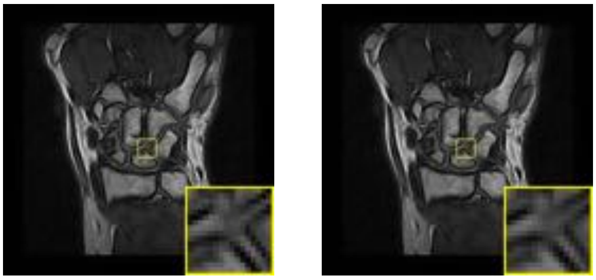

(d) Thin-Plate 256×256 $MRE=92.42, PSNR=28.47$ (e) Hardy 256×256 $MRE=90.26, PSNR=28.58$

Figure 2: *Image up-sampling and metrics induced by (c-e) different kernels. For all the images, (a) has been down-sampled to (b)* 128×128 *resolution and brought back to the initial* 256×256 *resolution.*

2.2. Morphological analysis of segmented images

Literature on 3D semi-automatic erosion detection is mainly focused on algorithms' validation against a reference value, obtained by the Omeract-Ramris scoring system [7]. Semi-automatic procedures aim to improve the reproducibility and sensitivity of the semi-quantitative scoring systems [70], and different methods [8, 5, 4, 51] have been validated on images and on surface meshes. High or low field MRIs can be used with negligible differences on erosion detection [27]. Leung *et al.* [51] proposed a global measures (e.g., volume) for monitoring the erosion progression. Comparing a sequence of bones acquired at different times with a reference atlas, they found an unexpected volume fluctuation in time, which does not identify a clear erosion as a matter of an inaccurate identification of the boundaries of segmented bones.

In [25], a semi-automated analysis of the carpal bones district from CT images is based on a segmentation that starts with a manually seeded edge detection and pro-

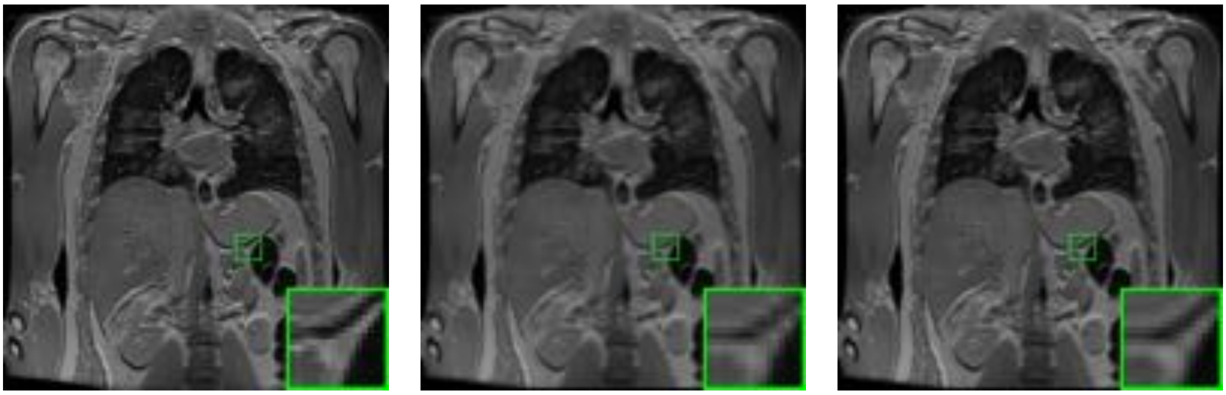

(a) Input 256×256 down-sampled to 128×128

(b) Bi-linear 256×256 $MRE = 284$, $PSNR = 23.60$

(c) Spline 256×256 $MRE = 277$, $PSNR = 23.70$

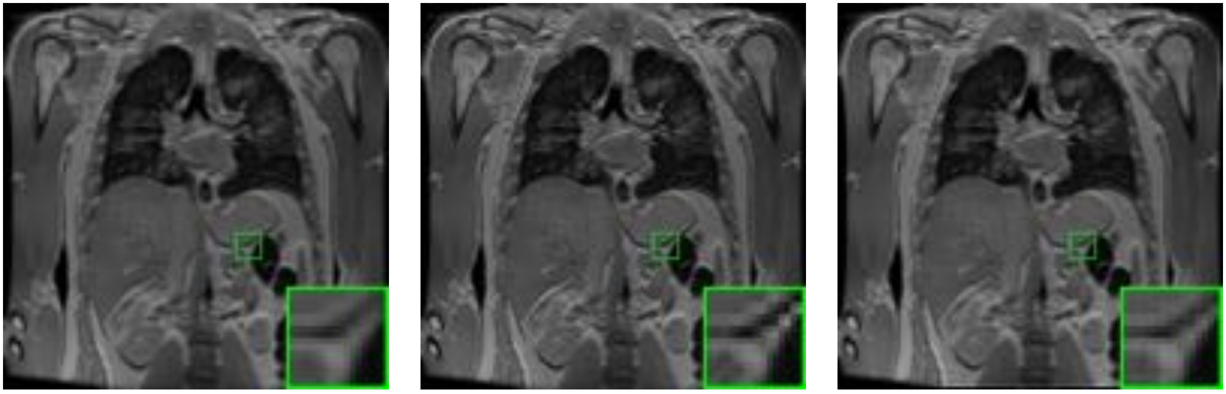

(d) RBF (Gauss) 256×256 $MRE = 136$, $PSNR = 26.70$

(e) RBF (Hardy) 256×256 $MRE = 151$, $PSNR = 24.20$

(f) RBF (Thin-plate) 256×256 $MRE = 146$, $PSNR = 25.30$

Figure 3: *Different up-samplings of a* 128×128 *image achieved as a downsampling of (a). The (b) bi-linear and (c) spline interpolation show a blurring effect over the whole image, (d) Gaussian and (e) Hardy kernels suffer from aliasing, as can be noticed on the contour of the shoulder, and thin-plate RBFs (f) provide a better up-sampling of the original image in (a). When the image is brought back to its original resolution, a blurring effect is associated with the bi-linear approximation and it is slightly reduced with a third order spline interpolator. The approximation with RBFs (d-f) provides a more definite image and preserves finer details.*

gresses with an automated active contour method. Multiple iterations of the active contour method on each slice produce the final segmentation. Indeed, the expert judgment has a crucial role in the discrimination of anatomical structures, especially if they are separated by weak boundaries. Local assessment is performed by monitoring only specific regions, which are identified as lesions. Cartilage damage assessment [32], which is useful for the early stage detection and monitoring of the disease, can be performed through the analysis of its thickness. Methods for the automatic estimation of the space narrowing and bone erosions are available for 2D X-Ray images [48] and 3D images (MRI or CT sequences) [51]. In [51], the automated approach shows a good correlation (0.80) with the same semi-automated procedure, but it is characterized by significant differences in the global bones' volume. For this reason, the expert judgment still has a crucial role in the discrimination of anatomical structures, especially if there are low-gradient structure boundaries in the image and regardless the use of segmented MRI data.

To train users of Omeract-Ramris, Ejbjerg *et al.* [27] developed an atlas with example images for the semi-quantitative scoring of synovitis, bone oedema, and erosion. Moving towards computer-aided assessments, Bird *et al.* [7] investigated the inter-reader reliability of computer-assisted (manual) erosion volume measurement in patients with rheumatoid arthritis and compared the results with the existing Omeract-Ramris scoring system. They found a strong positive correlation between the total erosion volumes and scores for all acquisitions, and a positive agreement between the man-

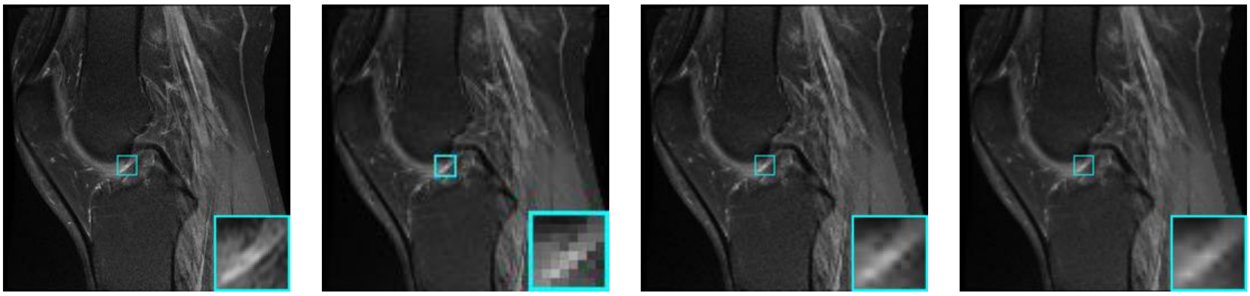

(a) 512×512 (b) 128×128 (c) Bi-linear 512×512 (d) RBF (Gauss) 512×512

Figure 4: *(b)* 128×128 *Down-sampling of (a) a high-resolution image and (b) up-sampling to the initial resolution with (c) bi-linear and (d) meshless (Gaussian kernel) approximations.*

ual evaluation of volumetric erosion by OsiriX [1] and the Omeract-Ramris classification. However, the inter-reader reliability was not sufficient to perform consistent multi-center studies, at least without a prior and homogeneous training of the users.

3. Local image up-sampling

Given a map $f:\mathcal{P}\rightarrow\mathbb{R}$, on a set $\mathcal{P}:=\{\mathbf{x}_i\}_{i=1}^{n}$ of points in $\mathbb{R}^d$, we propose a variant of the MLS scheme [52, 65, 64] for the computation of its underlying map $F:\mathbb{R}^d\rightarrow\mathbb{R}$, which is defined as a smooth function that *locally* approximates the f-values $\mathbf{f}:=(f(\mathbf{x}_i))_{i=1}^{n}$ (Fig. 1). For instance, for a 3D image $\{\mathbf{x}_i\}_{i=1}^{n}$ are the coordinates of the voxels, $f(\mathbf{x}_i)$ is the corresponding pixel intensity, and n is the total number of voxels in the image space. The idea behind our approach is to compute the function $F(\cdot)$ in a neighbor $\mathcal{N}_{\mathbf{x}}$ of $\mathbf{x}$ by imposing the f-values at $\mathcal{N}_{\mathbf{x}}$, instead of $\mathcal{P}$, as approximation constraints. In fact, the behavior of any continuous approximation of f at $\mathbf{x}$ is mainly controlled by the f-values in $\mathcal{N}_{\mathbf{x}}$.

3.1. Local MLS approximation with RBFs

We search the approximation $F(\cdot)$ in the linear space $\mathcal{F}$ generated by the radial basis functions $\{\phi_{j_s}(\mathbf{z}):=\phi(\|\mathbf{z}-\mathbf{x}_{j_s}\|_2)\}_{s=1}^{k}$ centered at the points of the neighbor $\mathcal{N}_{\mathbf{x}}:=\{\mathbf{x}_{j_s}\}_{s=1}^{k}$ of $\mathbf{x}$ and defined by the kernel ϕ. Let $W(\cdot,\cdot)$ be a strictly positive function and $\|\cdot\|_{\mathbf{W}(\mathbf{x})}$ the norm induced by the scalar product $\langle\mathbf{f},\mathbf{g}\rangle_{\mathbf{W}(\mathbf{x})}=\mathbf{f}^{\top}\mathbf{W}(\mathbf{x})\mathbf{g}$, $\mathbf{W}(\mathbf{x}):=\mathrm{diag}(W(\mathbf{x},\mathbf{x}_i))_{i=1}^{n}$. Then, the MLS approximation $F(\mathbf{x})=\sum_{s=1}^{k}\alpha_s(\mathbf{x})\phi_{j_s}(\mathbf{x})$ minimizes the energy

$$\begin{cases} E(\alpha):=\|\Phi\alpha(\mathbf{x})-\mathbf{f}\|_{\mathbf{W}(\mathbf{x})}^{2}, & \alpha(\mathbf{x}):=(\alpha_i(\mathbf{x}))_{i=1}^{k}, \\ \Phi:=(\phi_{ir})_{i=1,\dots,n}^{r=1,\dots,k}, & \phi_{ir}:=\phi_{j_r}(\mathbf{x}_i). \end{cases}$$

Deriving $E(\cdot)$ with respect to $\alpha(\mathbf{x})$, the normal equation

$$\left[\Phi^{\top}\mathbf{W}(\mathbf{x})\Phi\right]\alpha(\mathbf{x})=\Phi^{\top}\mathbf{W}(\mathbf{x})\mathbf{f}, \qquad (1)$$

depends on $\mathbf{x}$ and the points in $\mathcal{N}_{\mathbf{x}}$. Since the kernel ϕ is positive-definite, the $k\times k$ coefficient matrix $\Phi^{\top}\mathbf{W}(\mathbf{x})\Phi$ is positive definite; in particular, Eq. (1) has a unique solution. If the f-values are noise-free or have been smoothed, then we apply interpolating constraints by selecting $\Phi=(\phi_{ir})_{i,r=1}^{k}$ and $\mathbf{W}(\mathbf{x}):=\mathbf{I}$. Since the number of points in each neighbor is generally small, we select a kernel with a global support; i.e., the closure of the set of points where the kernel does not vanish is equal to $\mathbb{R}^{+}$. In our tests, we choose the Gaussian $\phi(t):=\exp(-t/\sigma)$ or bi-harmonic $\phi(t):=|t^3|/\sigma$ kernel, with support σ, and $W(\mathbf{x},\mathbf{y}):=\exp(-\|\mathbf{x}-\mathbf{y}\|_2)/\sigma$ is the Gaussian function. Enlarging the width of the kernel generally increases the robustness to noise and the approximation error.

Computational cost. The global approximation with RBFs requires the solution of one $n\times n$ system of linear equations for the whole data and then only a minimal amount of calculation is needed to evaluate the approximating function at any spatial location. In this case, the approximation with globally- and locally-supported RBFs takes $O(n^3)$ and $O(n\log n)$ time, respectively [38]. However, the allocation of the coefficient matrix and the numerical solver of the linear system for globally-supported RBFs represent a concrete bottleneck in all those applications where we deal with big data. Our approach requires the solution of a $k\times k$ linear system in $O(k^3)$ time, where k is a small constant (e.g., $20\leq k\leq 30$) that represents the average number of points in a given neighbor of a sample. This cost is comparable with the multi-level partition of the unity approximation [62], which applies a domain decomposition and solve only a linear system for each partitioning

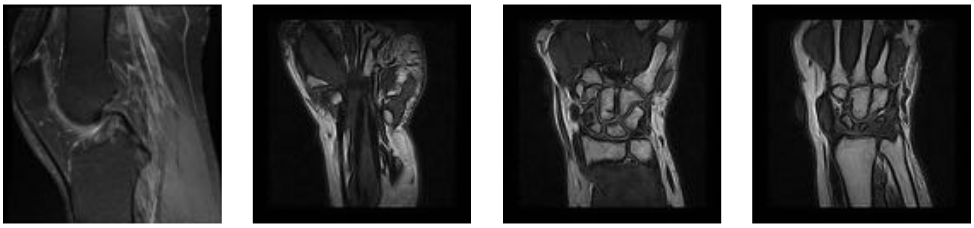

(a) 512×512 (b) 512×512 (c) 512×512 (d) 512×512

Figure	Error	Linear approx.	Polynomial approximation			RBF approximation			Feature-based, sparse & total variation approximations		
		$r=1$	$r=3$	$r=4$	$r=5$	Hardy	Gauss	Thin	FB Mean	LRTV	Sparse
2× **Downsampling & Up-sampling**											
(a)	MRE	43	41	41	41	**36**	37	51	36.10	36.12	36.09
	PSNR	31.73	31.95	31.94	31.93	**30.55**	32.39	31	31.02	30.55	31.54
	SSIM	0.84	0.85	0.85	0.85	**0.86**	0.85	0.84	0.84	0.84	0.83
(b)	MRE	70	62	61	61	**54**	59	55	54.31	54.52	54
	PSNR	29.68	30.19	30.22	30.23	**29.26**	30.42	30.68	29.62	29.30	29.26
	SSIM	0.87	0.88	0.88	0.88	**0.89**	0.88	0.89	0.85	0.84	0.89
(c)	MRE	113	102	102	101	**90**	97	92	92	91.04	90
	PSNR	27.57	28.01	28.04	28.05	**26.58**	28.23	28.47	27.20	26.71	26.59
	SSIM	0.85	0.85	0.85	0.85	**0.87**	0.85	0.86	0.86	0.84	0.87
(d)	MRE	105	94	93	93	**82**	87	83	82	82	82
	PSNR	27.88	28.39	28.42	28.43	**26.89**	28.71	28.91	26.90	26.91	28.89
	SSIM	0.86	0.87	0.87	0.87	**0.88**	0.87	0.88	0.88	0.88	0.88
4× **Downsampling & Up-sampling**											
(a)	MRE	94	91	91	92	**63**	64	2893	63.20	63	63.01
	PSNR	28.37	28.54	28.50	28.47	**27.90**	30.01	13.52	27.91	27.90	27.90
	SSIM	0.75	0.76	0.75	0.75	**0.79**	0.77	0.05	0.77	0.75	0.79
(b)	MRE	134	127	128	129	**127**	127	2115	127	127.29	127
	PSNR	26.85	27.08	27.05	27.02	**26.06**	27.09	27.88	27.01	27.05	26.10
	SSIM	0.79	0.79	0.79	0.78	**0.79**	0.79	0.81	0.79	0.75	0.79
(c)	MRE	207	201	204	205	**201**	202	2792	200	201	201
	PSNR	24.96	25.08	25.03	24.99	**24.09**	25.11	33.67	24.10	24.09	24.09
	SSIM	0.75	0.75	0.74	0.74	**0.75**	0.75	0.20	0.75	0.77	0.75
(d)	MRE	201	189	191	193	**184**	189	3132	185	186	184
	PSNR	25.09	25.35	25.31	25.27	**24.31**	25.35	25.17	24.42	24.31	24.33
	SSIM	0.76	0.77	0.76	0.76	**0.77**	0.77	0.21	0.77	0.77	0.75
8× **Downsampling & Up-sampling**											
(a)	MRE	196	206	210	212	**153**	160	2893	153	153	153
	PSNR	25.19	24.97	24.89	24.85	**23.27**	26.06	23.52	24.10	23.30	23.27
	SSIM	0.62	0.61	0.61	0.61	**0.63**	0.62	0.05	0.61	0.6	0.631
(b)	MRE	282	291	295	298	**273**	294	2115	273	273	273
	PSNR	23.63	23.49	23.42	23.38	**22.46**	23.44	24.88	22.50	24.90	22.47
	SSIM	0.69	0.68	0.68	0.67	**0.67**	0.67	0.21	0.65	0.67	0.67
(c)	MRE	389	420	430	435	**376**	421	2792	377	376	376
	PSNR	22.23	21.89	21.79	21.74	**21.62**	21.89	23.67	22.01	21.62	21.64
	SSIM	0.66	0.64	0.63	0.63	**0.64**	0.64	0.20	0.64	0.64	0.64
(d)	MRE	426	450	460	465	**421**	449	3132	439	421	422
	PSNR	21.83	21.59	21.50	21.45	**20.69**	21.61	1317	20.69	20.69	20.69
	SSIM	0.65	0.63	0.63	0.63	**0.64**	0.63	0.21	0.62	0.63	0.64

Table 1: *Statistics related to the* 2×, 4×, *and* 8× *image up-sampling of a set of (a-d) MR images with: (i) the local approximation induced by the Hardy, Gauss, and thin-plate kernels, (ii) linear and polynomial approximations of different order r, (iii) feature-based [44], sparse [56] and total variation [74] methods. For the local approximation with RBFs, the highest approximation accuracy is achieved with the Hardy's kernel, with slightly worse results when using the Gaussian kernel. Thin-plate kernel approximation does not work well for high resolution up-sampling (e.g.,* 4× *and* 8×*) due to the ill-conditioning of the corresponding coefficient matrix and the high smoothness of the resulting approximation. The proposed approach provides results comparable with the feature-based, sparse, and total variation methods. Best results are shown in bold.*

of the space and the linear/polynomial MLS approximations. Indeed, the proposed scheme has a lower computational cost until the number s of samples is lower than $n\log n/k^3$.

Continuity. To show the continuity of the local approximation scheme, let us assume that the entries of the weight matrix are bounded; i.e., $0 < a \leq W_i(\cdot) \leq b$. Since $F(\mathbf{x}) = \beta^\top(\mathbf{x})\tilde{\phi}(\mathbf{x})$ is a linear combination of continuous basis functions, we verify the continuity of $F(\cdot)$ at $\mathbf{x}$ by showing that $\beta(\cdot)$ is continuous at $\mathbf{x}$. The normal equations at $\mathbf{x}$ and $\mathbf{y}$ are given by

$$\begin{cases} [\Phi_{\mathbf{x}}^\top \mathbf{W}(\mathbf{x})\Phi_{\mathbf{x}}]\,\beta(\mathbf{x}) = \Phi_{\mathbf{x}}^\top \mathbf{W}(\mathbf{x})\mathbf{f}_{\mathbf{x}}, \\ [\Phi_{\mathbf{y}}^\top \mathbf{W}(\mathbf{y})\Phi_{\mathbf{y}}]\,\beta(\mathbf{y}) = \Phi_{\mathbf{y}}^\top \mathbf{W}(\mathbf{y})\mathbf{f}_{\mathbf{y}}. \end{cases} \qquad (2)$$

Applying the continuity of the weight matrix $\mathbf{W}(\mathbf{y})$ and of the basis functions at $\mathbf{x}$, from Eq. (2) it follows that $[\Phi_{\mathbf{x}}^\top \mathbf{W}(\mathbf{x})\Phi_{\mathbf{x}}]\lim_{\mathbf{y}\rightarrow\mathbf{x}}\beta(\mathbf{y}) = \Phi_{\mathbf{x}}^\top \mathbf{f}_{\mathbf{x}}$. We now show that the l_2 norm of $\beta(\mathbf{y})$ is bounded by a constant that is independent of $\mathbf{y}$. Firstly, we verify that

$$a\lambda_i(\Phi^\top\Phi) \leq \lambda_i(\Phi^\top\mathbf{W}(\mathbf{x})\Phi) \leq b\lambda_i(\Phi^\top\Phi), \qquad (3)$$

$i = 1,\ldots,k$, in fact, the Railegh quotient satisfies the relations

$$a\frac{\mathbf{v}^\top\Phi^\top\Phi\mathbf{v}}{\mathbf{v}^\top\mathbf{v}} \leq \frac{(\Phi\mathbf{v})^\top\mathbf{W}(\mathbf{x})(\Phi\mathbf{v})}{\mathbf{v}^\top\mathbf{v}} \leq b\frac{\mathbf{v}^\top\Phi^\top\Phi\mathbf{v}}{\mathbf{v}^\top\mathbf{v}}, \quad \mathbf{v}\in\mathbb{R}^k.$$

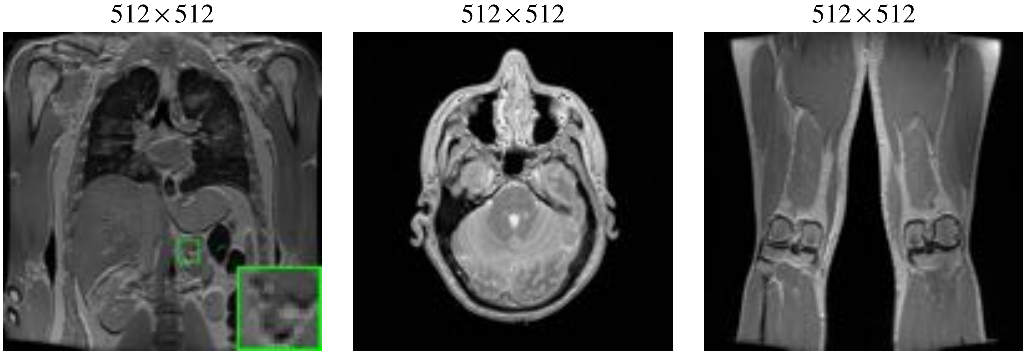

(a) (b) (c)

Figure	Error	**Linear approx.**	**Polynomial approx.**			**RBF approx.**			**Feature-based, sparse & total variation approx.**		
		$r=1$	$r=3$	$r=4$	$r=5$	Hardy	Gauss	Thin	FB Mean	LRTV	Sparse
2× **Downsampling & Up-sampling**											
(a)	MRE	116	108	108	108	**89**	94	108	90	90	91
	PSNR	27.46	27.77	27.77	27.76	**26.61**	28.40	27.76	26.61	26.90	27.01
	SSIM	0.81	0.82	0.82	0.82	**0.85**	0.83	0.82	0.84	0.83	0.83
(b)	MRE	216	203	203	203	**189**	199	199	190	189	189
	PSNR	24.78	25.05	25.05	25.04	**24.36**	25.13	25.13	24.37	24.40	24.36
	SSIM	0.86	0.86	0.85	0.86	**0.87**	0.85	0.85	87	87	87
(c)	MRE	110	101	101	101	**83**	86	98	84	83	83
	PSNR	27.70	28.05	28.05	28.05	**26.93**	28.78	28.18	27.01	27.00	26.98
	SSIM	0.86	0.87	0.87	0.87	**0.88**	0.87	0.85	0.86	0.87	0.88
4× **Downsampling & Up-sampling**											
(a)	MRE	211	199	201	202	188	**182**	5746	184	183	182
	PSNR	24.87	25.13	25.10	25.07	**24.37**	25.51	10.54	25.01	25.50	24.67
	SSIM	0.64	0.66	0.66	0.65	0.66	**0.67**	0.02	0.67	0.67	0.67
(b)	MRE	342	300	300	301	307	**298**	7754	300	299	299
	PSNR	22.79	23.35	23.35	23.33	**22.25**	23.30	9.24	22.28	22.25	22.25
	SSIM	0.76	0.77	0.77	0.77	**0.77**	0.77	0.45	0.75	0.75	0.77
(c)	MRE	197	177	177	178	168	**165**	6856	165	166	165
	PSNR	25.17	25.65	25.64	25.62	25.85	**25.05**	9.77	25.08	25.05	25.05
	SSIM	0.75	0.76	0.76	0.76	0.76	**0.76**	0.24	0.75	0.76	0.76
(c)	MRE	234	230	228	218	249	**230**	4838	235	266	260
	PSNR	26.34	26.65	28.64	29.62	25.13	**25.00**	39.44	25.08	27.06	25.05
	SSIM	0.35	0.36	0.36	0.36	0.36	**0.36**	0.34	0.35	0.36	0.36

Table 2: *Approximation accuracy of a* 2× *and* 4× *up-sampling of a (a-c) 3D MR images: best results are reported in bold. Statistics show a good performance of Hardy's approximation on average, with slightly worse results when using a Gaussian kernel. Thin-plate kernel approximation does not work well for high resolution up-sampling (e.g.,* 4×*) and the resulting approximation accuracy is analogous to splines, for any degree. The highest approximation accuracy is achieved with the local approximation with RBFs.*

Then, we get that

$$\begin{aligned}\|\beta(\mathbf{y})\|_2 &\leq_{\text{Eq. (2)}} b\lambda_1^{-1}(\Phi_{\mathbf{y}}^\top \mathbf{W}(\mathbf{y})\Phi_{\mathbf{y}})\|\Phi_{\mathbf{y}}^\top\|_2\|\mathbf{f}_{\mathbf{y}}\|_2\\ &\leq_{\text{Eq. (3)}} \lambda_1^{-1}(\Phi^\top\Phi)\lambda_n(\Phi)\|\mathbf{f}\|_2.\end{aligned}$$

Since the coefficient matrix $\Phi_{\mathbf{x}}^\top \mathbf{W}(\mathbf{x})\Phi_{\mathbf{x}}$ in Eq. (2) is invertible and $\lim_{\mathbf{y}\to\mathbf{x}}\beta(\mathbf{y})$ is finite, the uniqueness of the solution $\beta(\mathbf{x})$ to Eq. (2) guarantees that $\lim_{\mathbf{y}\to\mathbf{x}}\beta(\mathbf{y}) = \beta(\mathbf{x})$; i.e., $\beta(\cdot)$ is continuous at $\mathbf{x}$.

Finally, the ℓ_2 condition number of the coefficient matrix of the MLS approximation as

$$\begin{aligned}\kappa_2(\Phi^\top\mathbf{W}(\mathbf{p})\Phi) &= \frac{\lambda_{\max}(\Phi^\top\mathbf{W}(\mathbf{p})\Phi)}{\lambda_{\min}(\Phi^\top\mathbf{W}(\mathbf{p})\Phi)}\\ &\leq \frac{b}{a}\frac{\lambda_{\max}(\Phi^\top\Phi)}{\lambda_{\min}(\Phi^\top\Phi)} = \frac{b}{a}\kappa_2(\Phi^\top\Phi).\end{aligned}$$

3.2. Experimental results

We compare our approach with linear [80], spline [72, 79], local interpolation [59], feature-based [44], sparse [56], and total variation [74] methods on 2D and 3D MR images with low resolution. To evaluate the accuracy of the up-sampling scheme, we downsample a given image, bring it back to the initial resolution, and evaluate the differences between the original and the up-sampled images. The *mean square (residual) error* is defined as $MRE(A,B) := m^{-1}\sum_{i=1}^{m}(a_i - b_i)^2$, where A and B are two matrices with image intensities a_i and b_i, respectively, and m is the number of pixels. MRE range depends on the maximum intensity value λ in the image and lower values of MRE correspond to a higher similarity between images; e.g., in a grayscale image with values from 0 to $\lambda = 255$, MRE spans from 0 to λ^2. The *peak signal-to-noise ratio* $PSNR(A,B) := -10\log_{10}(\lambda^{-2}MRE(A,B))$ returns values in $[10,+\infty)$, which increase as the compared images become similar. The *structural similarly index* (SSIM) [82] mimics the human visual system and is independent of λ. It works on squared windows of the

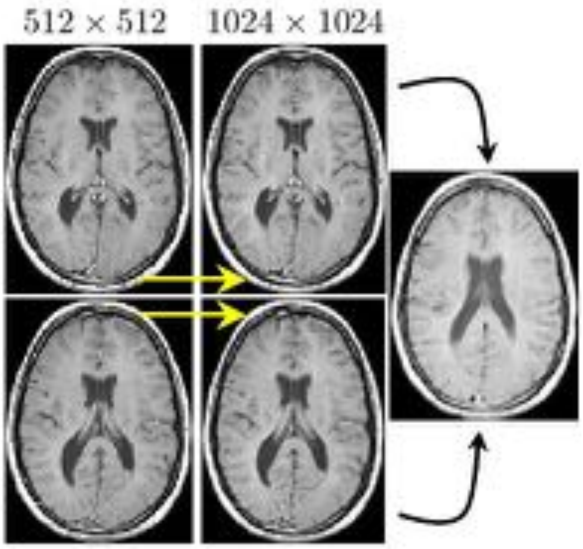

Figure 5: *Input images (first column) have been locally approximated with RBFs (second column) at a double resolution and the resulting approximation has been sampled on a new slice (right picture).*

images and returns a decimal value in $[-1, 1]$, where 1 corresponds to the case of two identical images.

In Fig. 2, the Hardy's kernel provides the best up-sampled image according to MRE and PSNR. In Fig. 3, the (b,c) bi-linear and spline interpolations show a blurring effect over the whole image, (d,e) Gaussian and Hardy kernels suffer from aliasing, as can be noticed on the contour of the shoulder, and thin-plate RBFs (f) provide a better up-sampling of the original image, in terms of details' preservation. In Fig. 4, the four-times image up-sampling (d) along each axis preserves finer details than the bi-linear interpolation (c), which tends to smooth out small-scale features of the input image.

Statistics (Tables 1, 2) show a good performance of Hardy's approximation on average with slightly worse results when using a Gaussian kernel. Thin-plate kernel approximation does not provide the same results in terms of quality, but it is on the same level of spline results, independently of the polynomial order. This result suggests a preference for third order splines, which perform faster than higher order splines. Linear approximation is worse than splines and requires less computational effort, but in some cases it can generate undesired effects, such as aliasing. Differences among the seven approaches are more emphasized for the first three sampled images. In the other cases, effects are attenuated, because MRI slices include wider and more homogeneous black areas. Moreover, thin-plate does not work well for extreme resolution up-sampling (e.g., 4× and 8×), as can be noticed in the last columns. The proposed approach also provides results that are comparable with the feature-based [44], sparse [56], and total variation [74] methods. An analogous discussion applies to the up-sampling of volumetric MR images, whose statistics (Table 3) with the minimum, maximum, and average PSNR, SSIM confirm the accuracy of the local approximation with RBFs.

(a) Non-local up-sampl. [59] 50×50

(b) RBF (Gauss) 50×50

Figure 6: $2\times$ *image up-sampling with (a) the non-local method* ($MRE = 13.44$; $PSNR = 36.27$) *and (b) RBF approximation (Gaussian kernel)* ($MRE = 13.65$; $PSNR = 33.87$)*, on a cerebral image.*

Comparing our approach (Fig. 6) with the non-local up-sampling [59], the latter exhibits a slightly better accuracy that is due to the more accurate up-sampling but requires a de-noising step and several iterations to optimize the image quality. Furthermore, these steps also raise computational complexity of the entire procedure.

Error	**Linear approx.**	**Polynomial approx.**			**RBF approx.**			**Feature-based, sparse & total variation approx.**		
	$r = 1$	$r = 3$	$r = 4$	$r = 5$	Hardy	Gauss	Thin	FB Mean	LRTV	Sparse
min PSNR	41.63	41.51	41.49	41.48	41.43	**41.25**	41.56	41.26	41.25	41.15
max PSNR	62.90	62.40	62.30	62.25	62.36	**62.10**	62.52	62.20	62.11	61.15
avg. PSNR	47.28	47.00	46.96	46.94	46.82	**46.27**	47.09	46.27	46.29	46.27
min SSIM	0.89	0.89	0.89	0.89	0.89	**0.89**	0.89	0.89	0.89	0.89
max SSIM	1.00	1.00	1.00	1.00	1.00	**1.00**	1.00	1.01	1.00	1.00
avg. SSIM	0.94	0.93	0.93	0.93	0.93	**0.86**	0.93	0.87	0.88	0.87

Table 3: *With reference to Fig. 3(a), metrics for different up-sampling methods applied to image series (intensity value range is [0, 65535]). the minimum, maximum, and average PSNR, SSIM values confirm the higher accuracy of the local approximation with RBF induced by the Gauss kernel. A sample slice of the image series is shown in Fig. 2(a). Best results are shown in bold.*

(a) Input im. 512×512 (b) Down-sampl. im. 256×256

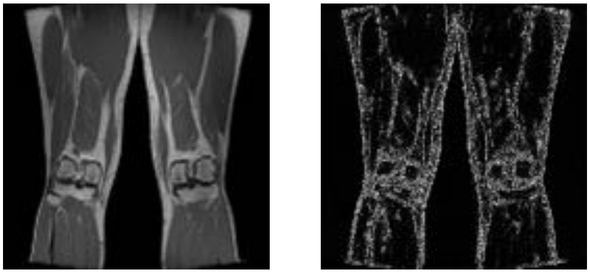

(c) Interp. im. 512×512 (d) Error 512×512

Figure 7: *(d) Squared difference between (a) the input images and (c) our local up-sampling with RBFs of the down-sampled image in (b); (d) the whiter pixels are, the higher is the discrepancy between (a) and (c).*

Through the proposed meshless approximation, we easily rescale the resolution of anisotropic images both on the image plane and inter-slices (Fig. 5). In this way, we further support the consistency of the approximation through a larger number of interpolating constraints across consecutive slices. Visualizing the point-wise approximation error as an image (Fig. 7), where the pixel intensity is the squared difference of the corresponding pixel values, the loss of information is mainly localized along the edges. However, in the up-sampled image, feature lines are accurately preserved as a matter of the interpolation constraints that guarantee a generally low approximation error, which is mainly due to the kernel smoothness.

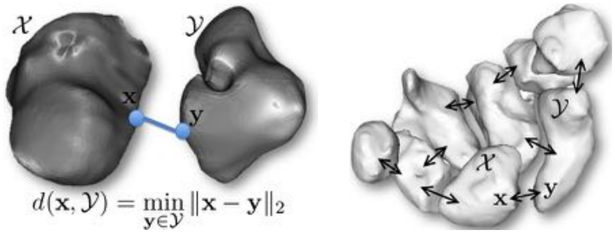

(a) (b)

Bone	**One-side Hausdorff distance**							
Capitate	-	10.2	58.3	-	44.2	-	13.6	57.4
Hamate	12.2	-	48.2	-	-	-	-	7.5
Lunate	58.2	48.2	-	-	17.3	-	-	60.3
Pisiform	-	-	-	-	-	-	-	44.7
Scaphoid	44.1	-	17.3	-	-	-	19.5	-
Trapezium	-	-	-	-	34.9	-	60.1	-
Trapezoid	12.7	-	-	-	19.6	60.1	-	-
Triquetal	57.2	7.5	60.4	44.1	-	-	-	-

(c)

Figure 8: *(a) One-side Hausdorff distance and (b) carpal bones. Arrows are a pictorial representations of distances. (c) Adjacency matrix for the wrist and intra-bones distance variation between the follow-up and the baseline.*

4. Morphological analysis of low-resolution and up-sampled MR images

In the following, we focus on the main aspects of the rheumatoid arthritis (Sect. 4.1), the morphological analysis of single scans (Sect. 4.2) and follow-up data (Sect. 4.3) from MR images of the hand-wrist sector.

4.1. MR images for the analysis of rheumatoid arthritis

This study is focused on the quantitative assessment of bone erosion in rheumatoid arthritis with MR images. We briefly recall that the rheumatoid arthritis is a chronic systemic disease that involves soft tissues (i.e., synovial tissue), cartilages, and bones of the peripheral joints. The temporal evolution of the disease is non-linear and the disease stages evolve from reversible to permanent, depending on the involved structures. The

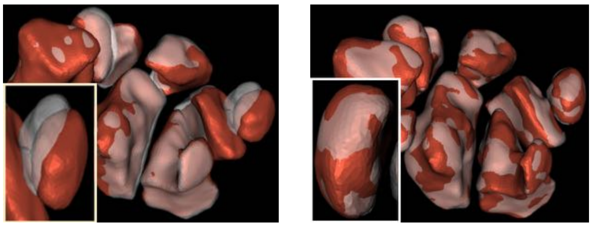

Figure 9: *ICP registration on (a) an entire wrist sector and (b) for each bone.*

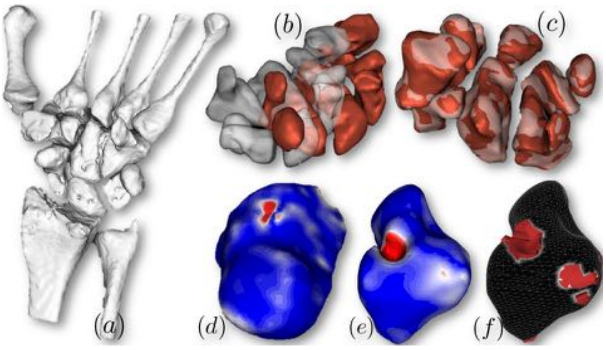

Figure 10: *(a) Segmented wrist district, (b) baseline (orange) and follow-up (grey) data, (c) co-registration. (d,e) Identification of local erosions of single bones and (f) eroded volume. The colormap varies from blue (lowest distance) to red (highest distance).*

stages of rheumatoid arthritis can be conceptually divided into two groups, without or with effects on the geometry of hard structures, such as bones and cartilages. In the first group, we include early stage inflammation, synovitis, and effusion; in the latter group, we consider the narrowing of joint space and erosion.

MR images generally show a good contrast among bones and surrounding tissues. In fact, bone erosion may be preceded by pathologies (e.g., inflammations, abnormalities) of the soft tissues by months or years [36]. These aspects and the low radiation associated with the acquisition of MR images show their importance for the early diagnosis and monitoring of the rheumatoid arthritis. A recent study [23] also demonstrates a correlation between erosion volumes detected by MR and CT, with MR that is capable of detecting 72% of the erosion detected by CT [30]. Since the cortical bone is detected as black in MR images and can be included in the eroded region, an overestimation of the eroded volume might affect the analysis with respect to CT [37], with a good inter-modality agreement between CT and MR on the volume of single erosions.

To measure the erosion score, we follow the standard OMERACT scoring system [28], which is based on the separate semi-quantitative evaluation of synovitis, bone edema, and bone erosion. Synovitis is assessed on a scale from 0 to 3 (none, mild, moderate, and severe), edema on a scale from 0 to 3 (none, one third, two thirds, and full), and erosions on a scale from 0 to 10 (none, 10%, 20%, 30%, ...). Bone erosion is also defined on the basis of images radiological appearance. To reduce some disadvantages of MR images (e.g., motion artifacts, aliasing artifacts, chemical shift artifacts), low-field local scans have been developed for the purpose of analyzing only a specific part of a limb. Finally, for our tests and as a ground truth, we have used the clinical database [77], which consists of low-field MRI images acquired from 30 patients affected by rheumatic arthritis and 10 healthy patients that have been segmented by rheumatologists.

4.2. Morphological analysis of single scans

The input to our process is a set of low-resolution and up-sampled MR images of complete joints, which are segmented with a geodesic active contour method [15] and are associated with a semantic label. For the carpal bones of the wrist district, the labels are: capitate, hamate, lunate, pisiform, scaphoid, trapezium, trapezoid, and triquetral. The proposed approach works on surface-based segmented data, while previous work is based mainly on volumetric data. For the analysis of a single exam (e.g., bone or complete joint), intra-bones distances are computed on the basis of anatomical atlases, where couples of neighbor bones are identified in the joint by the corresponding entries of an adjacency matrix (Fig. 8c). The *intra-bones distance* between two adjacent bones $\mathcal{X}$, $\mathcal{Y}$ is computed as $d(\mathcal{X},\mathcal{Y}) := \max\{d_{\mathcal{X}}(\mathcal{Y}), d_{\mathcal{Y}}(\mathcal{X})\}$, where $d_{\mathcal{X}}(\mathcal{Y}) := \max_{\mathbf{x}\in\mathcal{X}}\{\min_{\mathbf{y}\in\mathcal{Y}}\{\|\mathbf{x}-\mathbf{y}\|_2\}$ is the one-side Hausdorff distance. Each distance is then stored and compared with the following acquisitions to evaluate the joint space narrowing. Additional parameters of the input surface (e.g., curvature, roughness) can be extracted by applying geometric methods [4, 5] for the analysis of geometric surfaces.

4.3. Morphological analysis of follow-up data

The quantitative comparison between baseline and follow-up is performed by segmenting the individual bones, registering the segmented images, and calculating the distance between the corresponding segments. To this end, let us assume that our follow-up data set

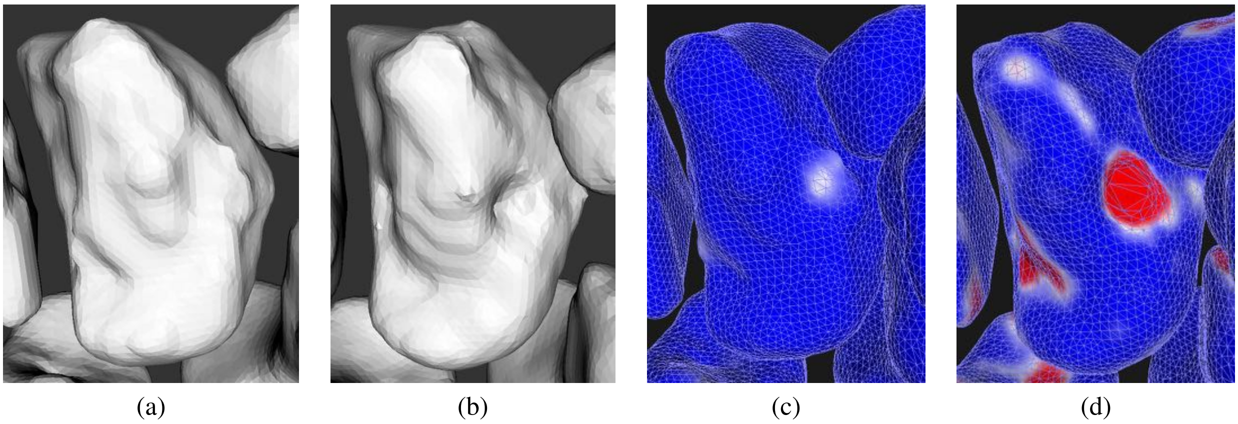

Figure 11: *Capitate with a large erosion on the (right) surface at the (a) baseline and (b) follow-up time; (c) identification of the erosion (white region) and (d) reconstruction of the missing volume (red region).*

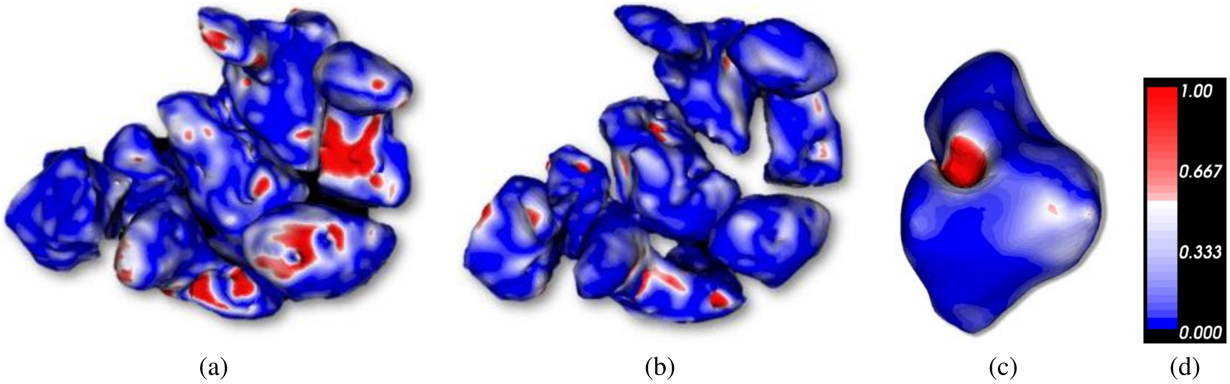

Figure 12: *(a,b) Local erosions of two wrist districts, (c) zoom-in of (a), and (d) color map.*

$\mathcal{R} := \{\mathcal{R}^j\}_{j=1}^{s}$ is represented as s segmented regions $\mathcal{R}^j$ of the same anatomical district, which have been acquired at different time steps $\{t_i\}_{i=1}^{s}$, $t_i < t_{i+1}$. Then, the segmented anatomical district is represented as the set $\mathcal{R}^j := \{R_i^j\}_{i=1}^{k_j}$, where each connected component R_i^j is a triangle mesh and is associated with its semantic label.

Co-registration of the anatomical sectors. Given two consecutive scans $\mathcal{R}^i$ and $\mathcal{R}^j$, the first issue to address is their misalignment, which is generally due to a different reference frame during the acquisition of the anatomical district. The registration of two scans of the same anatomical district can be based on the principal component analysis or the iterative closest point method [6, 19]. In the first case, we compute the reference frames $\mathcal{F}^i$, $\mathcal{F}^j$ of the two districts or of couples of corresponding bones (according to their label); then, we apply the translation and rotation that map $\mathcal{F}^j$ to $\mathcal{F}^i$ (Fig. 9a). In the latter case, the interior closest point (ICP) method minimizes a target function that measures the distance between $\mathcal{R}^i$, $\mathcal{R}^j$ (Fig. 9b). Even though both methods perform well, the ICP method has been selected for our analysis as it allows the user to properly tune the convergence parameters (e.g., maximum number of iterations, maximum tolerance). To avoid errors related to the joint mobility, the shape registration (Fig. 10(b,c)) is achieved by minimizing the ℓ_1 norm of each couple of corresponding bones in the baseline and follow-up.

Hausdorff distance of corresponding bones in two aligned scans. For the detection and quantification of local morphological variations (e.g., erosion) on a bone with respect to its baseline, we apply the two-side Hausdorff distance computed between the co-registered shapes. For each vertex of the baseline surface (Fig. 10(d,e)), the distance of the closest vertex of the follow-up surface is rendered according to a color

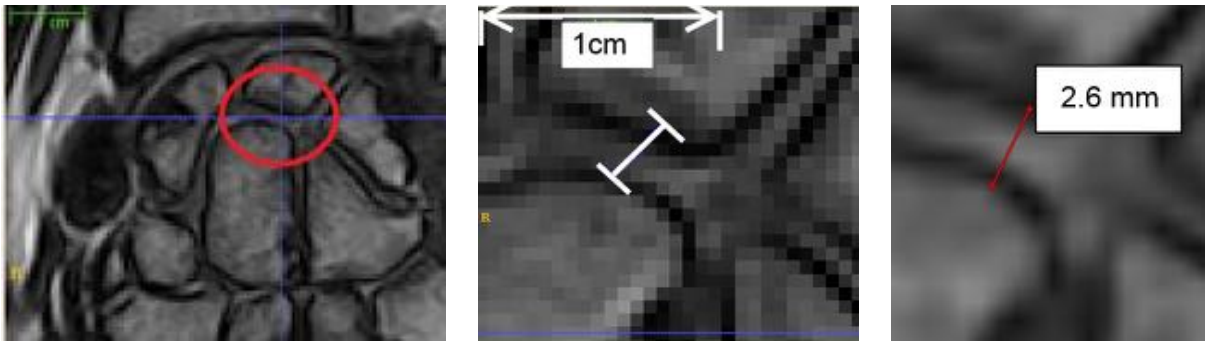

(a) (b) (c)

Figure 13: *Low field MRI* $(0.2T)$ *magnification. Image resolution* $256\times256\times104$*;* x,y,z *spacing* 0.55*mm*, 0.55*mm*, 0.60*mm. Coronal view (a) of carpal bones and non interpolated zoom on the capitate-lunate distance, (b) (ITK-SNAP [86]). Capitate-lunate distance (c) (*2.6*mm, RadiAnt DICOM Viewer [60]).*

map, where blue and red identify small and large distance values, respectively.

Analysis of the local erosion. The one-side Hausdorff distance provides a correspondence, which is not necessarily injective, between the point of $\mathcal{X}$ and $\mathcal{Y}$; in fact, each point $\mathbf{x}$ is assigned to the point $\mathbf{y}\in\mathcal{Y}$ such that $\mathbf{y}=\arg\min\{d(\mathbf{x},\mathbf{z}),\,\mathbf{z}\in\mathcal{Y}\}$. Exploiting this correspondence, a set of "eroded parts" is built on the baseline shape by coupling the vertices of each triangle of the baseline surface with the corresponding closest vertices of the follow-up surface. Then, the volume of each eroded part is computed and gives a quantitative local information that is less affected by the global variability of the pipeline (Figs. 10(f), 11). This information on the position of the eroded regions (Fig. 12), their area and volume variation are annotated in the segmentation. To identify the zones with larger erosion, the values of the Hausdorff distance are mapped onto the baseline (or follow-up) geometry by means of a color map. A set of "missing parts", corresponding to the eroded volumes, is visualized on the baseline shape.

4.4. Experimental results

We now discuss the morphological analysis of low-resolution and up-sampled MR images of the hand-wrist sector and affected by musculo-skeletal pathologies.

Pipeline repeatability assessment on the hand-wrist district. To evaluate the variability associated with the user-guided segmentation process, we consider a set of low-resolution MR images (0.20 Tesla, $256\times256\times104$; x,y,z spacing 0.55 mm, 0.55 mm, 0.60 mm) and a rough estimation of the error in the intra-joint distance computation is derived as follow. According to Fig. 13, the distance between capitate and lunate corresponds to a minimum of 3 and a maximum of 5 pixels crossed diagonally. Since each pixel crossed diagonally measures 0.78*mm*, the associated distance can vary between 2.34*mm* and 3.90*mm*. Considering the voxels' dimension, the relative errors for intra-bones distance and global volume evaluation are about ±15% and ±25%, respectively.

Inter-observer and intra-observer agreements of global bone volume computation were evaluated with a data set of 117 and 32 bones, respectively. Three expert users segmented all the bones, and results were compared and analyzed by Bland-Altman statistics [9]. Inter-observer agreement analysis for each couple (user$_i$ *vs.* user$_j$), $i,j=1,2,3$, gives biases and confidence bounds $(\pm1.96\cdot\sigma)$ of $-0.5\pm20.0\%$, $-18.1\pm27.2\%$, $-11.1\pm29.6\%$. Intra-observer agreement analysis gives limits of agreement $(\pm1.96\cdot\sigma)$ of $-3.2\pm19.5\%$ for user$_1$, $0.7\pm16.5\%$ for user$_2$, and $-4.2\pm13.3\%$ for user$_3$, user$_2$. Given the geometric complexity and scale of the wrist sector, we conclude that this variability is due to the image quality; in fact, these results are in agreement with the evaluation of the relative errors based on image.

Follow-up volume variation and joint space narrowing. A set of 120 bones (15 wrists), segmented by an expert in rheumatoid arthritis and acquired from 5 different patients, was analyzed to check if the global bone volume and the intra-bones distance (related to joint space narrowing) can be correlated to the disease evolution, in terms of erosion progression, assuming that erosion pro-

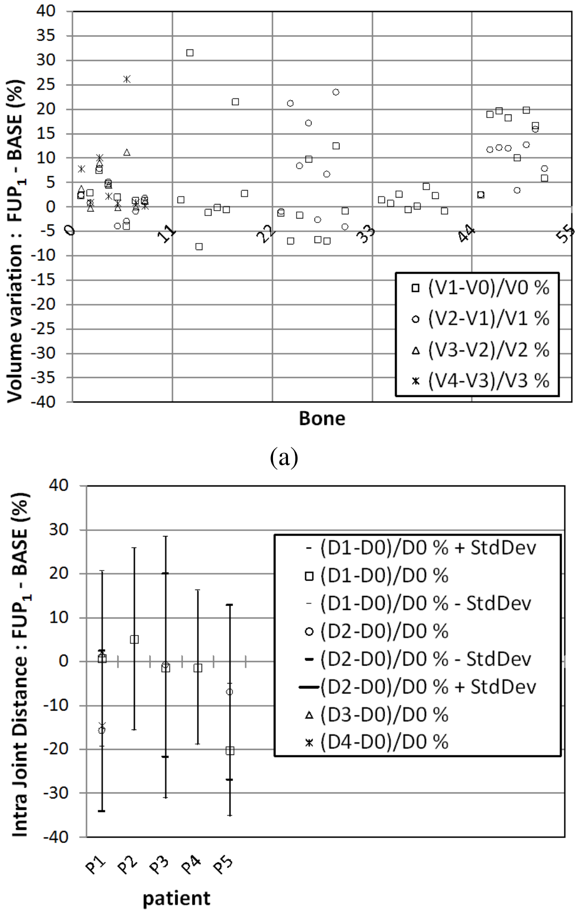

(a)

(b)

Figure 14: *(a) Bone volume variations and (b) joint space narrowing for each follow-up exam for carpal bones. V_i and D_i are the volume and distance at the i-th temporal acquisition, respectively.*

duce a global volume reduction. For each bone, volume variations are computed with respect to the baseline acquisition (i.e., earliest exam); a negative value indicates a reduction in the bone volume. Results are dispersed (Figs. 14(a), 15(a)) and the mean value for the volume variation is $(+1.76 \pm 10.71\%)$. In these experiments, the *statistical significance of the results* is $p = 0.89$ and it reflects the difficulties of operating on complex and low-resolution data already noted in the data variability analysis.

Intra-bones distance variations were evaluated on the same data set, to check if this measure is able to track the joint space narrowing evolution (connected to bone erosion, also in the early stages of the disease), assuming that the intra joint distance decreases in time, as typical of the rheumatoid arthritis. On the basis

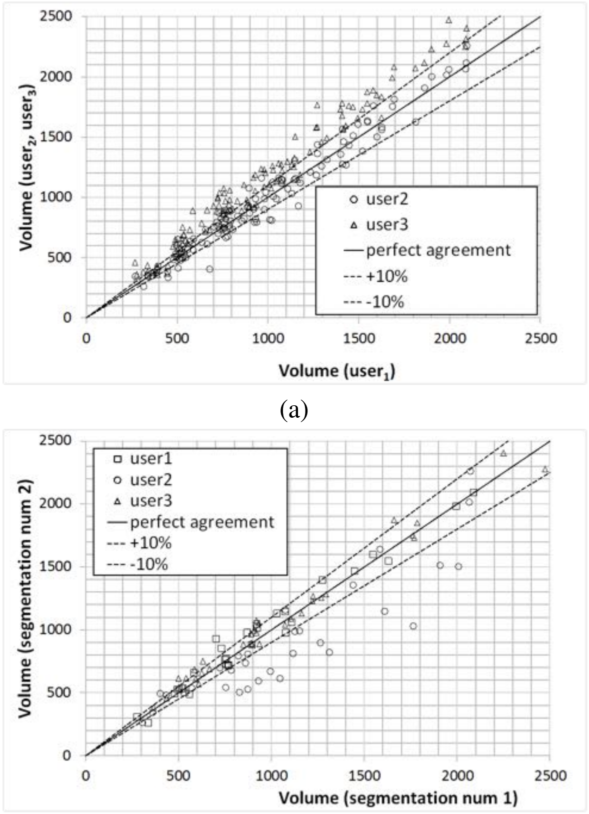

(a)

(b)

Figure 15: *(a) Inter-observer agreement. Data and line of equality for the volume of bones segmented by user$_1$ vs user$_2$ (circles) and vs user$_3$ (triangles). (b) Intra-observer agreement. Data and line of equality for the volume of bones segmented by each user (1st vs 2nd measurement). user$_1$ (squares), user$_2$ (circles) and user$_3$ (triangles).*

of an anatomical atlas, the adjacency matrix for the wrist sector (Fig. 8) was used to couple neighbor bones. Fig. 14(b) shows the mean distance variation for each wrist sector with reference to its corresponding baseline exam (Fig. 15(b)). Each point on the graph represents the mean of the distance variations of a complete joint acquired at a time following the baseline, and the corresponding confidence bound. The global mean value $(\pm\sigma)$ is $-5.3 \pm 8.1\%$. Also in this case the check of statistical significance is critical, as we obtained a $p = 0.64$.

Morphological analysis of up-sampled MR images. Image up-sampling allows us to achieve a more accurate segmentation and quantitative analysis of morphological parameters of segmented 3D anatomical districts from low field MR images, reduce the effect of volume variability, and improve the consistency of the

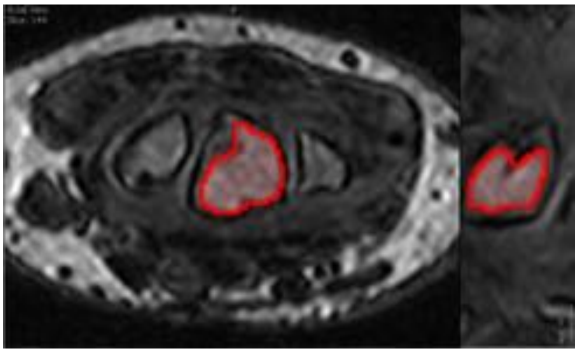

(a) $128 \times 128 \times 51$

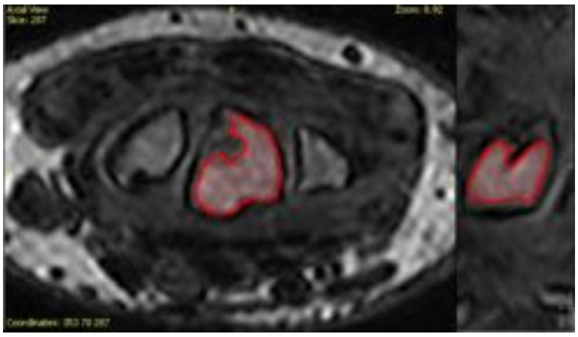

(b) $256 \times 256 \times 102$

Figure 16: *Single bone segmentation. Two views (a) of a slice are compared with the two corresponding views (b) of the up-sampled image. The image up-sampling facilitates the selection of the seed points of small bones and tiny cartilage for a more detailed and reliable segmentation with the geodesics-active contour.*

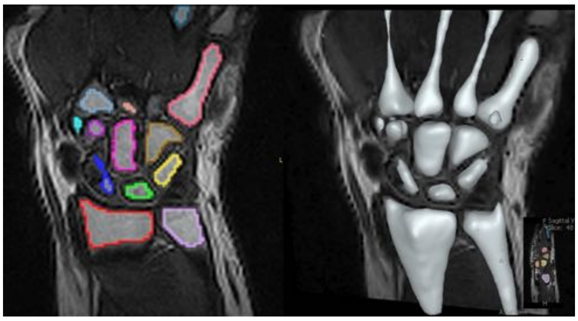

$128 \times 128 \times 51$

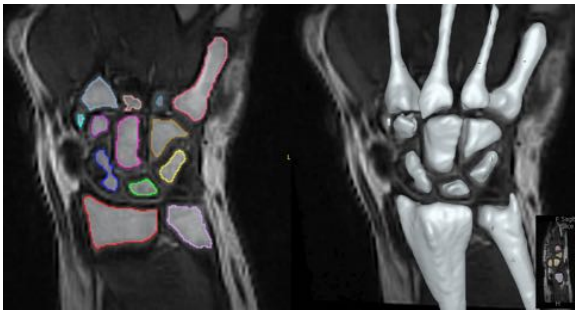

$256 \times 256 \times 102$

Figure 17: *Segmentation of an MR 3D image: coronal view to the left side and 3D rendering to the right. The upper image corresponds to a volume with resolution* $128 \times 128 \times 51$*, whereas the lower image is its RBF up-sampled version, with resolution* $256 \times 256 \times 102$*.*

results for follow-up data. To this end (Fig. 16), a MR image $128 \times 128 \times 51$ has been up-sampled to a finer $256 \times 256 \times 102$ resolution and the comparison is conducted setting the same segmentation parameters for the low- and high-resolution images. The segmentation algorithm works better on higher resolution images because it penetrates higher frequency features more easily and can reach the segmented object boundaries more closely. Main improvements (Figs. 12, 17) after up-sampling include a higher precision along contours (from left image) and reliability of the morphology of the segmented bones (right image). Due to a higher precision in the identification of the seed voxel used by the segmentation with geodesic active contours, we avoid segmentation errors, such as spurious connected components (first upper bone on the right), which are typically induced by a wrong selection of the seed in low resolution images.

Our preliminary results on the comparison of the segmentation of up-sampled MR images of the hand-wrist sectors of 10 patients affected by rheumatoid arthritis with the corresponding ground-truth [77] show (i) a higher precision (23.5%) in the identification of the seed voxel used by the segmentation with geodesic active contours; (ii) a higher precision (19.5%) of the segmented contours and less smoothed bones; and (iii) a lower number (21%) of segmentation errors (e.g., spurious connected components) that are typically induced by a wrong selection of the seed pixels.

5. Conclusions and future work

We have proposed a local moving least-squares approximation with radial basis functions for the up-sampling of low resolution MR images; in this case, the volumetric and meshless properties of the approximation allow us to easily process images with anisotropic voxel size by rescaling the image and inter-slices resolution. This up-sampling method has been used to support a more accurate segmentation and quantitative analysis of morphological parameters of segmented 3D anatomical districts.

Morphological characterization can provide valuable indicators to be used in clinical assessments and in studies

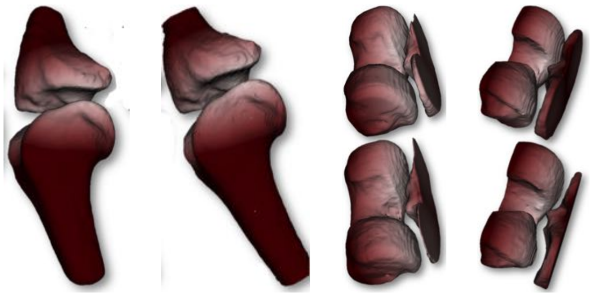

(a) (b) (c) (d)

Figure 18: *Knee joint and intra-bones distance (femur ↔ tibia) mapped in different postures. (a,c)* 0° *and (b,d)* 80°*. The colormap varies from white (lowest distance) to red (highest distance).*

on large populations. By this characterization, an automatic analysis of large data sets can be carried out, thus addressing inter-observer agreement issues and saving experts' time. The mandatory prerequisite for the use of these procedures is a significant validation against experts' evaluation with a reference scoring system (e.g., for rheumatoid arthritis, the RAMRIS). The morphological analysis of the local erosion can be useful to compare qualitatively and quantitatively segmented data, and to aid the identification of eroded or locally modified regions.

The morphological characterization of segmented data is general enough to be applied to different anatomical districts for the identification of artifacts in the acquired data, the analysis of the effects of degenerative pathologies of soft and bony tissues, and the localization of shape variations due to posture. Initial tests have been performed on knee sectors from low field MR images (0.25 Tesla; x,y,z spacing: 0.70 mm, 0.70 mm, 0.90 mm), acquired at two different postures, with a joint angle of 0° and 80°, and segmented by an expert. The evaluated variation of the intra-bones distances on two scans of the knee district of four patients shows a homogeneous reduction $(-24.0 \pm 22\%)$ for the 80° posture with respect to the 0° posture. The distances between adjacent structures is mapped on the bones (Fig. 18) and the quantification of their variation is useful to characterize different diseases, such as cartilage destruction or other pathologies involving a geometrical modification of the joint structures. Finally, as future work we plan to validate both the image up-sapling method and the morphological analysis on a larger data set, also involving medical doctors and radiologist for a clinical validation of the results.

Acknowledgements. Special thanks are given to the Reviewers for their valuable comments, which helped us to improve the presentation and experimental description of the proposed approach. This work has been partially supported by the MIUR-Regione Liguria Research Project "*TEDIG: Technologies for Ecographics Diagnosis*". Low-field MR images and segmented data are courtesy of the *Visible Human Project*, DIMI-UNIGE, POLITECMED (Regional Hub for Biomedical Technologies), and SOFTECO Srl, Genova - Italy.

References

[1] O. Ratib A. Rosset, L. Spadola. Osirix: an open-source software for navigating in multidimensional DICOM images. *Journal of Digital Imaging*, 17(3):205–216, 2004.

[2] J. Allebach and P.W. Wong. Edge-directed interpolation. In *Intern. Conference on Image Processing*, volume 3, pages 707–710 vol.3, Sep 1996.

[3] L.E. Andersson and T. Elfving. Interpolation and approximation by monotone cubic splines. *Journal of Approximation Theory*, 66(3):302–333, 1991.

[4] I. Banerjee, A. Agibetov, C. E. Catalano, G. Patanè, and M. Spagnuolo. Semantics-driven annotation of patient-specific 3D data: a step to assist diagnosis and treatment of rheumatoid arthritis. *The Visual Computer*, pages 1–13, 2016.

[5] I. Banerjee, C. E. Catalano, G. Patanè, and M. Spagnuolo. Semantic annotation of 3D anatomical models to support diagnosis and follow-up analysis of musculoskeletal pathologies. *Int. Journal Computer Assisted Radiology and Surgery*, 11(5):707–720, 2016.

[6] P.J. Besl and Neil D. McKay. A method for registration of 3D shapes. *IEEE Trans. on Pattern Analysis and Machine Intelligence*, 14(2):239–256, 1992.

[7] P. Bird, B. Ejbjerg, F. McQueen, M. Ostergaard, M. Lassere, and J. Edmonds. OMERACT Rheumatoid Arthritis Magnetic Resonance Imaging Studies. *The Journal of rheumatology*, 30(6):1380–4, 2003.

[8] P. Bird, M. Lassere, R. Shnier, and J. Edmonds. Computerized measurement of magnetic resonance imaging erosion volumes in patients with rheumatoid arthritis: a comparison with existing magnetic resonance imaging scoring systems and standard clinical outcome measures. *Arthritis Rheum.*, 3(48):614–624, 2003.

[9] J. M. Bland and D. G. Altman. Statistical methods for assessing agreement between two methods of clinical measurement. *The Lancet*, 327(8476):307 – 310, 1986.

[10] J. Bloomenthal and B. Wyvill, editors. *Introduction to Implicit Surfaces*. Morgan Kaufmann Publishers Inc., 1997.

[11] N.K. Bose and N.A. Ahuja. Superresolution and noise filtering using moving least-squares. *IEEE Trans. on Image Processing*, 15(8):2239–2248, 2006.

[12] D. Cai, X. He, K. Zhou, J. Han, and H. Bao. Locality sensitive discriminant analysis. In *Proc. of the 20th International Joint Conference on Artifical Intelligence*, pages 708–713. Morgan Kaufmann Publishers Inc., 2007.

[13] W.K. Carey, D.B. Chuang, and S.S. Hemami. Regularity-preserving image interpolation. *IEEE Trans. on Image Processing*, 8(9):1293–1297, 1999.

[14] J. C. Carr, R. K. Beatson, J. B. Cherrie, T. J. Mitchell, W. R. Fright, B. C. McCallum, and T. R. Evans. Reconstruction and

representation of 3D objects with radial basis functions. In *ACM Siggraph*, pages 67–76, 2001.

[15] V. Caselles, R. Kimmel, and G. Sapiro. Geodesic active contours. *Intern. Journal of Computer Vision*, 22(1):61–79, 1997.

[16] R. Castillo, E. Castillo, R. Guerra, V. E. Johnson, T. McPhail, A. K. Garg, and T. Guerrero. A framework for evaluation of deformable image registration spatial accuracy using large landmark point sets. *Physics in Medicine and Biology*, 54(7):1849, 2009.

[17] S.G. Chang, Z. Cvetkovic, and M. Vetterli. Resolution enhancement of images using wavelet transform extrema extrapolation. In *Intern. Conference on Acoustics, Speech, and Signal Processing*, volume 4, pages 2379–2382 vol.4, 1995.

[18] M.J. Chen, C.H. Huang, and W.L. Lee. A fast edge-oriented algorithm for image interpolation. *Image and Vision Computing*, 23(9):791–798, 2005.

[19] Y. Chen and G. Medioni. Object modelling by registration of multiple range images. *Image and Vision Computing*, 10(3):145 – 155, 1992.

[20] P. Cignoni, C. Rocchini, and R. Scopigno. Metro: Measuring error on simplified surfaces. *Computer Graphics Forum*, 17(2):167–174, 1998.

[21] T. Cresson, B. Godbout, D. Branchaud, R. Chav, P. Gravel, and J.A. de Guise. Surface reconstruction from planar x-ray images using moving least squares. In *Intern. Conference of the IEEE Engineering in Medicine and Biology Society*, pages 3967–3970, Aug 2008.

[22] P.E. Danielsson and M. Hammerin. High-accuracy rotation of images. *Graphical Models and Image Processing*, 54(4):340–344, 1992.

[23] U.F. Dohn, B.J. Ejbjerg, M. Hasselquist, and et al. Detection of bone erosions in rheumatoid arthritis wrist joints with magnetic resonance imaging, computed tomography and radiography. *Arthritis Research & Therapy*, 10:R25, 2008.

[24] W. Dong, L. Zhang, G. Shi, and X. Wu. Image deblurring and super-resolution by adaptive sparse domain selection and adaptive regularization. *Trans. on Image Processing*, 20(7):1838–1857, July 2011.

[25] J. Duryea, M. Magalnick, S. Alli, L. Yao, M. Wilson, and R. Goldbach-Mansky. Semiautomated three-dimensional segmentation software to quantify carpal bone volume changes on wrist CT scans for arthritis assessment. *Medical Physics*, 35(6):2321–2330, 2008.

[26] N. Dyn, D. Levin, and S. Rippa. Numerical procedures for surface fitting of scattered data by radial functions. *SIAM Journal on Scientific and Statistical Computing*, 7(2):639–659, 1986.

[27] B. Ejbjerg, F. McQueen, M. Lassere, E. Haavardsholm, P. Conaghan, P. O'Connor, P. Bird, C. Peterfy, J. Edmonds, M. Szkudlarek, H. Genant, P. Emery, and M. O Stergaard. The Eular-Omeract rheumatoid arthritis MRI reference image atlas: the wrist joint. *Annals of the rheumatic diseases*, pages 23–47, 2005.

[28] B Ejbjerg, F McQueen, M Lassere, E Haavardsholm, P Conaghan, P O'Connor, P Bird, C Peterfy, J Edmonds, Marcin Szkudlarek, et al. The eular–omeract rheumatoid arthritis MRI reference image atlas: the wrist joint. *Annals of the rheumatic diseases*, 64(suppl 1):i23–i47, 2005.

[29] M. Elad and D. Datsenko. Example-based regularization deployed to super-resolution reconstruction of a single image. *The Computer Journal*, 52(1):15–30, 2009.

[30] A.X. Falcao, J.K. Udupa, S. Samarasekera, and S. Sharma. User-steered image segmentation paradigm: live wire and live lane. *Graphics Models and Image Processing*, 60:233–260, 1998.

[31] R Farwig. Multivariate interpolation of arbitrarily spaced data by moving least squares methods. *Journal of Computational and Applied Mathematics*, 16(1):79–93, 1986.

[32] J. Folkesson, E. Dam, O. Fogh Olsen, P. Pettersen, and C. Christiansen. Automatic segmentation of the articular cartilage in knee MRI using a hierarchical multi-class classification scheme. *Inter. Conference on Medical image computing and computer-assisted intervention*, 8:327–34, 2005.

[33] D. H. Frakes, L. P. Dasi, K. Pekkan, H. D. Kitajima, K. Sundareswaran, A. P. Yoganathan, and M. J. T. Smith. A new method for registration-based medical image interpolation. *IEEE Trans. on Medical Imaging*, 27(3):370–377, March 2008.

[34] S. Fuhrmann and M. Goesele. Floating scale surface reconstruction. *ACM Trans. on Graphics*, 33(4):46:1–46:11, July 2014.

[35] P. Ghosh, M. Mitchell, J. A. Tanyi, and A. Y. Hung. Incorporating priors for medical image segmentation using a genetic algorithm. *Neurocomputing*, 195:181 – 194, 2016. Learning for Medical Imaging.

[36] G. Gilkenson, R. Polisson, H. Sinclair, and et al. Early detection of carpal erosions in patients with reumathoid arthritis: a pilot study of magnetic resonance imaging. *Rheumatology*, 15:1361–1366, 1989.

[37] R. Goldbach-Mansky, V. Mahadevan, L. Yao, and P. E. Lipsky. The evaluation of bone damage in rheumatoid arthritis with magnetic resonance imaging. *Clinical and experimental rheumatology*, 21(5 Suppl 31):S50–3, 2003.

[38] G. Golub and G.F. VanLoan. *Matrix Computations*. John Hopkins University Press, 2nd Edition, 1989.

[39] A. Goshtasby, D.A. Turner, and L.V. Ackerman. Matching of tomographic slices for interpolation. *IEEE Trans. on Medical Imaging*, 11(4):507–516, 1992.

[40] G.J. Grevera and J.K. Udupa. Shape-based interpolation of multidimensional grey-level images. *IEEE Trans. on Medical Imaging*, 15(6):881–892, 1996.

[41] G.J. Grevera and J.K. Udupa. An objective comparison of 3D image interpolation methods. *IEEE Trans. on Medical Imaging*, 17(4):642–652, Aug 1998.

[42] G.J. Grevera, J.K. Udupa, and Y. Miki. A task-specific evaluation of three-dimensional image interpolation techniques. *IEEE Trans. on Medical Imaging*, 18(2):137–143, Feb 1999.

[43] B.K. Gunturk, Y. Altunbasak, and R.M. Mersereau. Multiframe resolution-enhancement methods for compressed video. *IEEE Signal Processing Letters*, 9(6):170–174, 2002.

[44] K. Jafari-Khouzani. MRI upsampling using feature-based nonlocal means approach. *IEEE Trans. on Medical Imaging*, 33(10):1969–1985, Oct 2014.

[45] K. Jafari-Khouzani. MRI upsampling using feature-based nonlocal means approach. *IEEE Trans. on Medical Imaging*, 33(10):1969–1985, 2014.

[46] K. Jensen and D. Anastassiou. Subpixel edge localization and the interpolation of still images. *IEEE Trans. on Image Processing*, 4(3):285–295, 1995.

[47] H. Kirshner and M. Porat. On the role of exponential splines in image interpolation. *IEEE Trans. on Image Processing*, 18(10):2198–2208, Oct 2009.

[48] G. Langs, P. Peloschek, H. Bischof, and F. Kainberger. Automatic quantification of joint space narrowing and erosions in rheumatoid arthritis. *IEEE Trans. on Medical Imaging*, 28(1):151–64, 2009.

[49] Y.J. Lee and J. Yoon. Nonlinear image upsampling method based on radial basis function interpolation. *IEEE Trans. on Image Processing*, 19(10):2682–2692, 2010.

[50] C. Lessig, M. Desbrun, and E. Fiume. A constructive theory of sampling for image synthesis using reproducing kernel bases. *ACM Trans. on Graphics*, 33(4):55:1–55:14, July 2014.

[51] K. K. Leung, M. Holden, N. Saeed, K. J. Brooks, J. B. Buckton,

A. Williams, S. P. Campbell, K. Changani, D. G. Reid, Y. Zhao, M. Wilde, D. Rueckert, J. V. Hajnal, and D. L. G. Hill. Automatic quantification of changes in bone in serial MR images of joints. *IEEE Trans. on Medical Imaging*, 25(12):1617–26, 2006.

[52] D. Levin. The approximation power of moving least-squares. *Mathematics of Computation*, 67(224):1517–1531, 1998.

[53] M. Li and T.Q. Nguyen. Markov random field model-based edge-directed image interpolation. *IEEE Trans. on Image Processing*, 17(7):1121–1128, 2008.

[54] X. Li and M.T. Orchard. New edge directed interpolation. In *Intern. Conference on Image Processing*, volume 2, pages 311–314 vol.2, 2000.

[55] X. Liu, D. Zhao, R. Xiong, Siwei M., W. Gao, and H. Sun. Image interpolation via regularized local linear regression. *IEEE Trans. on Image Processing*, 20(12):3455–3469, Dec 2011.

[56] X. Lu, Z. Huang, and Y. Yuan. MR image super-resolution via manifold regularized sparse learning. *Neurocomputing*, 162:96 – 104, 2015.

[57] Zhenhua M., J. Rajan, M. Verhoye, and J. Sijbers. Robust edge-directed interpolation of magnetic resonance images. In *Intern. Conference on Biomedical Engineering and Informatics*, volume 1, pages 472–476, Oct 2011.

[58] J. V. Manjón, P. Coupé, A. Buades, D. L. Collins, and M. Robles. MRI superresolution using self-similarity and image priors. *Journal of Biomedical Imaging*, 2010:17:1–17:11, January 2010.

[59] J.V. Manjón, P. Coupé, A. Buades, V. Fonov, D.L. Collins, and M. Robles. Non-local MRI upsampling. *Medical Image Analysis*, 14(6):784–792, 2010.

[60] Medixant. Radiant dicom viewer. copyright © 2009-2013 medixant., 2013.

[61] C. A. Micchelli. Interpolation of scattered data: distance matrices and conditionally positive definite functions. *Constructive Approximation*, 2:11–22, 1986.

[62] Y. Ohtake, A. Belyaev, M. Alexa, G. Turk, and H.-P. Seidel. Multi-level partition of unity implicits. *ACM Siggraph*, 22(3):463–470, 2003.

[63] S.C. Park, M.K. Park, and M.G. Kang. Super-resolution image reconstruction: a technical overview. *IEEE Signal Processing Magazine*, 20(3):21–36, 2003.

[64] G. Patanè. Multi-resolutive sparse approximations of d-dimensional data. *Computer Vision and Image Understanding*, 117(4):418–428, 2013.

[65] G. Patanè, M. Spagnuolo, and B. Falcidieno. Topology- and error-driven extension of scalar functions from surfaces to volumes. *ACM Trans. on Graphics*, 29(1):1–20, 2009.

[66] G.P. Penney, J.A. Schnabel, D. Rueckert, M.A. Viergever, and W.J. Niessen. Registration-based interpolation. *IEEE Trans. on Medical Imaging*, 23(7):922–926, 2004.

[67] M. Protter, M. Elad, H. Takeda, and P. Milanfar. Generalizing the nonlocal-means to super-resolution reconstruction. *IEEE Trans. on Image Processing*, 18(1):36–51, 2009.

[68] S.P. Raya and J.K. Udupa. Shape-based interpolation of multidimensional objects. *IEEE Trans. on Medical Imaging*, 9(1):32–42, Mar 1990.

[69] S. S. Rifman. Digital rectification of ERTS multispectral imagery. *In Proceedings of Symposium Significant Results Obtained from ERTS-I*, 1:1131–1142, 1973.

[70] Hodgson R.J. and Moots R. O'Connor P. MRI of rheumatoid arthritis image quantitation for the assessment of disease activity, progression and response to therapy. *Rheumatology*, 1(47):13–21, 2008.

[71] F. Rousseau. A non-local approach for image super-resolution using intermodality priors. *Medical Image Analysis*, 14(4):594 – 605, 2010.

[72] I.J. Schoenberg. Cardinal interpolation and spline functions: II interpolation of data of power growth. *Journal of Approximation Theory*, 6(4):404–420, 1972.

[73] C. Shen, J. F. O'Brien, and J. R. Shewchuk. Interpolating and approximating implicit surfaces from polygon soup. In *ACM Siggraph Courses*, page 204, 2005.

[74] F. Shi, J. Cheng, L. Wang, P. T. Yap, and D. Shen. LRTV: Mr image super-resolution with low-rank and total variation regularizations. *IEEE Trans. on Medical Imaging*, 34(12):2459–2466, 2015.

[75] F. Shi, L. Wang, G. Wu, G. Li, J.H. Gilmore, W. Lin, and D. Shen. Neonatal atlas construction using sparse representation. *Human Brain Mapping*, 35(9):4663–4677, 2014.

[76] M. Srinivas, R. Ramu Naidu, C.S. Sastry, and C. Krishna Mohan. Content-based medical image retrieval using dictionary learning. *Neurocomputing*, 168:880 – 895, 2015.

[77] V. Tomatis, M. A. Cimmino, F. Barbieri, G. Troglio, P. Parascandolo, L. Cesario, G. Viano, L. Vosilla, M. Pitikakis, and A. Schiappacasse. A database of segmented MRI images of the wrist and the hand in patients with rheumatic diseases. In *New Trends in Image Analysis and Processing–ICIAP 2015 Workshops*, pages 143–150. Springer, 2015.

[78] G. Turk and J. F. O'Brien. Modelling with implicit surfaces that interpolate. *ACM Siggraph*, 21(4):855–873, 2002.

[79] M. Unser. Splines: A perfect fit for signal and image processing. *IEEE Signal Processing Magazine*, 16(6):22–38, 1999.

[80] M. Unser, A. Aldroubi, and M. Eden. Enlargement or reduction of digital images with minimum loss of information. *IEEE Trans. on Image Processing*, 4(3):247–258, 1995.

[81] Y. Wang, Z. Zhang, and B. Guo. 3D image interpolation based on directional coherence. In *IEEE Workshop on Mathematical Methods in Biomedical Image Analysis*, pages 195–202, 2001.

[82] Z. Wang, A.C. Bovik, H.R. Sheikh, and E.P. Simoncelli. Image quality assessment: From error visibility to structural similarity. *IEEE Trans. on Image Processing*, 13(4):600–612, 2004.

[83] H. Wendland. Real piecewise polynomial, positive definite and compactly supported radial functions of minimal degree. *Advances in Computational Mathematics*, 4(4):389–396, 1995.

[84] C. Xu, D. Tao, and C. Xu. Large-margin multi-viewinformation bottleneck. *IEEE Trans. on Pattern Analysis and Machine Intelligence*, 36(8):1559–1572, Aug 2014.

[85] J. Yang, J. Wright, T. Huang, and Y. Ma. Image super-resolution as sparse representation of raw image patches. In *IEEE Conference on Computer Vision and Pattern Recognition*, pages 1–8, June 2008.

[86] P. A. Yushkevich, J. Piven, H. C. Hazlett, R. G. Smith, S. Ho, J. C. Gee, and G. Gerig. User-guided 3D active contour segmentation of anatomical structures: Significantly improved efficiency and reliability. *Neuroimage*, 31(3):1116–1128, 2006.

[87] Di Zhang, Jiazhong He, Yun Zhao, and Minghui Du. MR image super-resolution reconstruction using sparse representation, nonlocal similarity and sparse derivative prior. *Computers in Biology and Medicine*, 58:130 – 145, 2015.

[88] Y. Zhang, G. Xu, and C. Bajaj. Quality meshing of implicit solvation models of biomolecular structures. *Computer Aided Geometric Design*, 23(6):21, 2006.